Structure of $DyFe_2/YFe_2$ Laves phase superlattices grown by molecular beam epitaxy

2003 J. Phys.: Condens. Matter 15 6493

(http://iopscience.iop.org/0953-8984/15/38/017)

INSTITUTE OF PHYSICS PUBLISHING JOURNAL OF PHYSICS: CONDENSED MATTER

J. Phys.: Condens. Matter **15** (2003) 6493–6512 PII: S0953-8984(03)61592-4

Structure of $DyFe_2/YFe_2$ Laves phase superlattices grown by molecular beam epitaxy

M J Bentall[1], **R C C Ward, E J Grier and M R Wells**

Oxford Physics, Clarendon Laboratory, Parks Road, Oxford OX1 3PU, UK

E-mail: m.bentall1@physics.ox.ac.uk

Received 21 March 2003, in final form 20 June 2003
Published 12 September 2003
Online at stacks.iop.org/JPhysCM/15/6493

Abstract

The crystal structure of a series of six high quality single crystal Laves phase superlattice samples, of structure $[t_1$ Å $DyFe_2/t_2$ Å $YFe_2]_N$, grown by molecular beam epitaxy have been probed using a high resolution triple crystal x-ray diffractometer. A study of the scattering near the 2 2 0, 4 4 0 and 2 6 $\bar{2}$ reflections has revealed the presence of several superlattice peaks, showing that the samples exhibit a high degree of superlattice modulation. The typical mosaic spread is less than 0.9°, while the superlattice coherence lengths are typically 2000 Å. Fitting of a model to the data using a differential evolution algorithm with a Rietveld refinement has confirmed the high quality of these samples and shows that the interface widths are typically ∼20 Å. Measurements of the in-plane and out-of-plane lattice parameters show that the samples are subjected to a shear that is slightly anisotropic in the plane. Transverse scans through the Bragg and superlattice peaks show that the width is mainly dominated by a mosaic crystal effect, with a small contribution arising from the correlated roughness at the bilayer interfaces. Finally, high resolution electron microscopy images show directly that these superlattices exhibit a high degree of modulation.

(Some figures in this article are in colour only in the electronic version)

1. Introduction

There is considerable interest in the magnetic properties of Laves phase superlattices. This stems partly from a practical point of view and partly from a fundamental point of view. Firstly, these structures present, theoretically at least, the possibility of developing hard magnets whose performance parameter, the magnetic energy product $(BH)_{MAX}$, is as large as 1 MJ m^{-3}, provided that the exchange spring mechanism can be suppressed [1]. This is important because, at present, the energy product available with modern magnets is sufficiently close to the theoretical limits that a new method will be required if higher performance magnets are

[1] Author to whom any correspondence should be addressed.

to be made. Secondly, the research on Laves phase thin layers and superlattices is a natural extension of the 1970s research on the bulk Laves phases [2] and of the more recent studies on rare earth superlattices [3–6].

The recent interest in the magnetic behaviour of Laves phase superlattices has shown using magnetization measurements the existence of a variety of magnetic properties and structures in these systems. These superlattices are composite systems of hard and soft magnetic materials, where the magnetization of the hard material is usually tied to an easy direction, whereas the magnetization of the soft magnetic material can in some cases be turned by the application of an external magnetic field.

In the $DyFe_2$–YFe_2 superlattices, the $DyFe_2$ layers consist of dysprosium and iron moments coupled antiparallel, forming a ferrimagnet through the effective exchange interaction. The YFe_2 layers are also ferrimagnetic, but the yttrium site only has a small induced moment [7], while the iron moments tend to align parallel to one another as a result of the strong Fe–Fe exchange interaction. Finally, there is a weak coupling of the dysprosium moments giving long range parallel alignment of the dysprosium moments. When these materials are combined into superlattices there are clearly a wide variety of magnetic configurations possible, a result of the above magnetic interactions, the artificial periodicity of the superlattice, the epitaxially induced magnetic anisotropy and the interaction of the structure with any applied magnetic field.

Recent studies have shown the existence of the so-called spring magnet behaviour [8, 9]. This behaviour arises when the magnetization of the $DyFe_2$ layers dominates the structure, with the result that the easy direction of magnetization is largely determined by these layers. The iron moments in the YFe_2 layers couple parallel to those in the $DyFe_2$ layers through the strong exchange interaction. If a magnetic field is applied above a critical bending field, the iron moments in the YFe_2 layers tend to rotate parallel to the field direction to reduce their Zeeman energy.

Another interesting magnetic structure that arises is when the magnetization of the YFe_2 layers dominates the magnetic structure. In this case, when a magnetic field is applied it can be favourable for the iron moments in the YFe_2 layers to all align parallel to the field while the net moment in the $DyFe_2$ layers is antiparallel to the applied field direction. This behaviour has been shown to be the source of negative coercivity in some samples [10–14].

Finally these structures have been shown to exhibit giant magnetoresistance properties. A change in resistance, $\Delta R/R$, of 32% has been demonstrated in an applied field of 23 T [15].

The explanation of these effects relies heavily on the superlattice structure exhibiting a high degree of modulation between the hard and soft magnetic layers. Therefore in this study we have investigated the structure of six superlattice samples using x-ray diffraction and high resolution electron microscopy (HREM) techniques. By simulating the x-ray scattering longitudinal lineshape, we are able perform a simultaneous non-linear least squares fit of a model to the scattering around three Bragg reflections using a differential evolution algorithm (DEA) and thereby deduce the average lattice parameters, the number of layers in the YFe_2 and $DyFe_2$ blocks of the superlattice and the concentration profile and interface widths of the bilayer. Resolution corrected measurements of the width of the main Bragg reflection in the growth direction allow an estimate of the superlattice coherence length, ξ, to be made. The transverse lineshape through the main Bragg peak and superlattice peaks have also been measured and, from this, the structure of the planes parallel to the growth direction is deduced.

2. Sample growth

Bulk $DyFe_2$ and YFe_2 crystallize in a face centred cubic diamond structure with eight RFe_2 units per cubic unit cell. The structure is made up of a tetrahedron of iron atoms surrounded

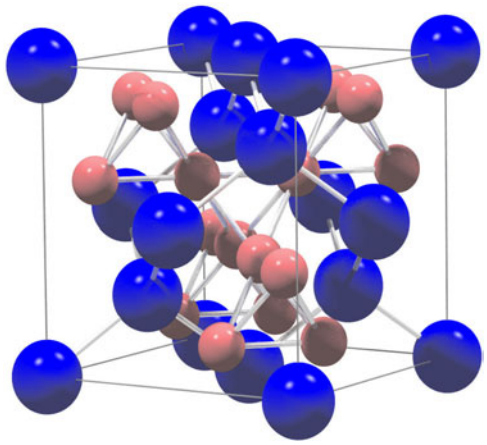

Figure 1. The cubic unit cell of the C15 Laves phases $DyFe_2$ and YFe_2. The large spheres represent dysprosium or yttrium atoms and the small spheres represent iron atoms. They crystallize in the face centred cubic structure O_h^7 ($Fd\bar{3}m$) with 24 atoms per cubic unit cell.

by the rare earth atoms and is schematically illustrated in figure 1. These compounds have bulk lattice parameters of 7.325 and 7.363 Å respectively [2]. The samples were grown using a molecular beam epitaxy (MBE) facility. Sapphire substrates with a (1 1 $\bar{2}$ 0) orientation were used and 1000 Å of (1 1 0) niobium was deposited as a chemical buffer layer, followed by a 20 Å thick iron 'seed' to improve crystal growth [16]. The iron seed layer is thought to improve the epitaxial growth because of an interaction that occurs between the iron atoms with the niobium interface, that creates a surface intermetallic phase. RHEED patterns observed during this stage of growth show that the alloy is deposited as a two dimensional rectangular lattice in agreement with [16] and referred to as NbFe-φ. The superlattice was then grown by co-deposition of the elementary fluxes and grows with [1 1 0] as the growth direction. Six superlattice samples of structure $[t_1$ Å $DyFe_2/t_2$ Å $YFe_2]_N$ were grown and the growth process was monitored *in situ* using RHEED diffraction.

The best samples were found to grow with an initial growth temperature of 600 °C for the superlattice, which was subsequently reduced to 450 °C over the course of the first few bilayer repeats. The epitaxial relationships are [1 1 $\bar{2}$ 0] sapphire ∥ [1 1 0] Laves, [0 0 0 1] sapphire ∥ [1 $\bar{1}$ 1] Laves and [$\bar{1}$ 1 0 0] sapphire ∥ [$\bar{1}$ 1 2] Laves. The schematic structure of the samples is shown in figure 2.

The sample thickness was estimated by calibrating the fluxes immediately before the sample growth using a quartz crystal monitor located exactly at the substrate position. Control systems maintained stable fluxes throughout the growth, allowing the thickness of the layer to be determined from the growth time. This estimate of the layer thickness is referred to as the nominal thickness. The nominal sample structures are given in table 1, along with some of their structural properties.

3. Experimental analysis

3.1. X-ray scattering

The structure of the superlattices has been investigated using a triple crystal Philips MRD high resolution x-ray diffractometer with an incident wavelength of 1.540 56 Å from a copper target.

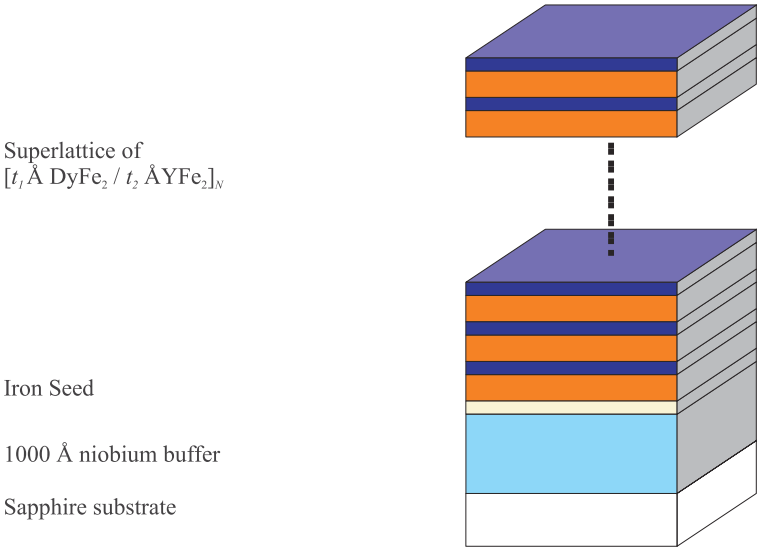

Figure 2. A schematic view of a Laves phase superlattice of structure [t_1 Å DyFe$_2$/t_2 Å YFe$_2$]$_N$ grown by MBE.

Table 1. Some structural parameters of the DyFe$_2$/YFe$_2$ superlattices as determined by x-ray diffraction at room temperature. The parameters given in the table were obtained by fitting the data to a Pearson VII function using a conventional Levenberg–Marquardt fitting routine. ξ is the superlattice coherence length and Υ is the rocking curve FWHM. Sample 1002 is a 10 000 Å thick layer of DyFe$_2$.

Sample	Nominal structure	Υ (deg)	ξ (Å)
932	$[100/100]_{40}$	0.755(0.002)	2300(200)
933	$[150/150]_{40}$	0.92(0.01)	3600(300)
955	$[250/150]_{30}$	0.82(0.01)	1200(100)
989	$[70/30]_{60}$	0.987(0.001)	1800(200)
990	$[50/70]_{60}$	0.874(0.002)	1700(200)
1003	$[150/100]_{50}$	0.850(0.002)	2300(200)
1002	10 000 Å DyFe$_2$	0.812(0.001)	—

A four bounce germanium (2 2 0) monochromator, with a 0.5° diverging slit, and a 0.3 × 4.0 mm crossed slit assembly gave a primary beam divergence of better than 12 arcsec. Most of the experiments were performed in a two crystal configuration, with a secondary slit size of 0.5 mm. The resolution function was estimated by measuring $1\,1\,\bar{2}\,0$, $2\,2\,\bar{4}\,0$ and $2\,2\,\bar{4}\,\bar{6}$ sapphire peaks close to the 2 2 0, 4 4 0 and $2\,\bar{6}\,2$ superlattice reflections. This enabled the resolution function to be estimated at each of these three peaks as $(\Delta q_x, \Delta q_z) = (6, 8) \times 10^{-4}$, $(6, 8) \times 10^{-4}$ and $(20, 8) \times 10^{-4}$ Å^{-1} respectively. Selected measurements around the 2 2 0 superlattice reflection were also performed in a three crystal configuration and the resolution was again estimated from the measurement of the $1\,1\,\bar{2}\,0$ sapphire reflection as $\Delta q = 5.0 \times 10^{-4}$ Å^{-1} in the scattering plane.

All the data were taken at room temperature. The scattering vector, $\boldsymbol{Q}$, was varied parallel and perpendicular to the layer surface, through the centre of the Bragg or satellite peak. These scans were defined by two components, $q_z \parallel [1\,1\,0]$ and $q_x \parallel [1\,\bar{1}\,1]$. Scans in which q_x were varied are referred to as transverse scans while those in which q_z varied are referred

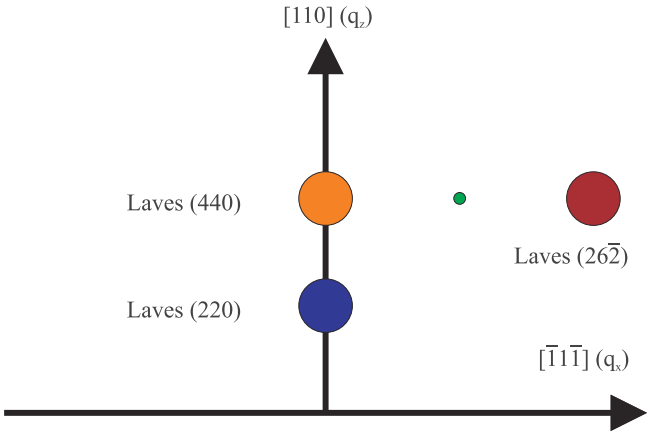

Figure 3. A schematic diagram showing the region of reciprocal space probed in the x-ray scattering experiments.

to as longitudinal scans. The Bragg reflections are given in the usual Miller index notation $h\,k\,l$, where each of the indices is related to the q components and the lattice parameters as $q_z = (2\pi/a)\sqrt{h^2+k^2}$, with $h = k$, and $q_x = (2\pi/a)\sqrt{h^2+k^2+l^2}$, with $h = \bar{k} = l$. The scattering was measured around 2 2 0, 4 4 0, 2 6 $\bar{2}$, figure 3, and in addition for some samples the 6 6 0 and 1 7 $\bar{3}$ reflections were also measured.

4. Theory of scattering from superlattices

Superlattices may exhibit a wide variety of defects that can modify the superlattice structure from the ideal; figure 2. The nature of the defects is dependent upon many factors including the substrate, growth temperature and constituent elements. Usually, *in situ* analysis such as RHEED diffraction can be used as an initial guide to the superlattice quality, but more precise techniques such as x-ray diffraction analysis or HREM are needed to quantitatively determine it.

Defects in superlattices may be broadly be divided into two categories. Firstly, there may be variations of the structural parameters in the growth direction. This can arise because of fluctuations in the interlayer spacing or number of planes, or interdiffusion between the individual blocks of a bilayer. The second type of defect arises if the planes perpendicular to the growth direction are imperfect. This can be due to interfacial roughness that distorts the flat interfaces which furthermore can be (a) correlated, (b) cumulative and (c) uncorrelated roughness. Correlated roughness arises when most bumps or troughs in an interface are reproduced in the next, with the result that the imperfect interface is propagated throughout the entire superlattice. Cumulative roughness arises when there are excess atoms in one region and each time a new layer is deposited the excess increases, with the result that any bump in the superlattice is amplified as the superlattice structure is built up [17, 18]. These types of roughness are schematically illustrated in figure 4.

HREM and x-ray scattering measurements presented here show that the roughness of the Laves phase superlattices is mainly correlated. For the x-ray scattering measurements, this type of roughness is also evidenced by the fact that the widths of the transverse scans through main Bragg reflection and satellites are approximately constant. This observation means that any model of the longitudinal profile can be greatly simplified, effectively to a one dimensional model.

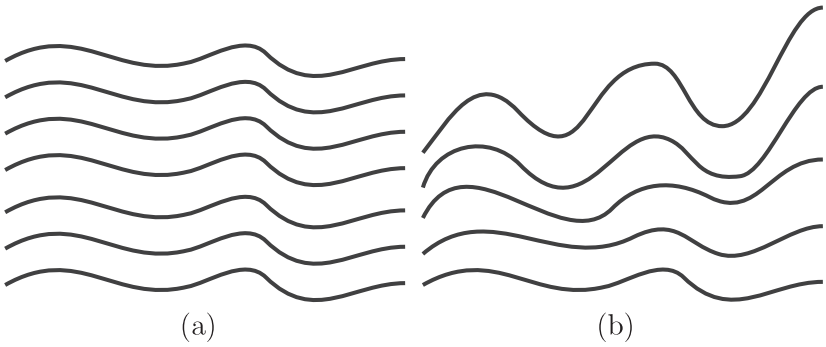

Figure 4. A schematic view of (a) correlated and (b) cumulative roughness that may be present in a superlattice sample.

4.1. Longitudinal profile

In the kinematical approximation, the intensity for elastic charge scattering of x-rays is given by

$$I(\boldsymbol{Q}) \propto \left| \sum_l f_l(\boldsymbol{Q}) \mathrm{e}^{\mathrm{i}\boldsymbol{Q}\cdot\boldsymbol{R}_l} \right|^2, \tag{1}$$

where $\boldsymbol{Q}$ is the wavevector transfer, $\boldsymbol{R}_l$ is the position of the lth atom and the sum is performed over all atoms in the sample. $f_l(\boldsymbol{Q})$ is the atomic form factor and is given in the *International Tables for Crystallography* [19]. Equation (1) is often applied to superlattices by assuming that the bilayer repeat distance, $\bar{\Lambda}$, is constant and that the structures of all bilayers are identical. This implies that $\bar{\Lambda}$ is an integral number of atomic layers. Then averaging over the atomic layers perpendicular to the growth direction:

$$I(q_z) \propto \left| \left(\sum_{S=0}^{N-1} \mathrm{e}^{\mathrm{i}q_z \bar{\Lambda} S} \right) \left(\sum_{l=0}^{n_1+n_2-1} f_l(q_z) \mathrm{e}^{\mathrm{i}q_z z_l} \right) \right|^2, \tag{2}$$

where there are N bilayers of width $\bar{\Lambda}$ and n_1 and n_2 are the number of planes of each constituent. The first term in this equation give rise to a series of peaks when $q_z = (2\pi M)/\bar{\Lambda}$ with M as an integer. Since however the strongest intensity usually occurs close to the Bragg reflections of the bulk material it is convenient to write this as

$$q_z = \frac{2\pi l}{\bar{d}} + \frac{2\pi m}{\bar{\Lambda}}, \tag{3}$$

where $m = 0, \pm 1, \pm 2, \ldots$ is the order of the satellite. The second term is known as the bilayer structure factor and is the envelope function that modifies the intensity of the peaks of the first term. This approach has been the basis for the analysis of many superlattice systems [3, 5, 6].

The difficulty with this approach is that it requires that the bilayer has an integral number of atomic planes and since during the growth there are no RHEED oscillations it is impossible to control the growth such that this requirement is satisfied. This is a particularly severe problem when there are several different planes stacked along the growth direction. For example, the growth of a FCC structure on (1 1 1) planes requires the regular deposition of planes in an ... ABC ABC ABC ... sequence. The bilayer must then contain exactly $3n$ planes if each bilayer is to be identical. The stacking sequence of close-packed planes for growing HCP structures on the (0 0 1) planes is ... AB AB AB ... and the bilayer must then be $2n$ planes. The structure of the Laves phases grown on (1 1 0) planes consists of three planes. There are

planes B containing only iron atoms and planes A and C that both contain equal numbers of rare earth (dysprosium or yttrium) and iron atoms. The difference between A and C is that the positions of the atoms differ like those of the AB planes in the FCC structure. The structure of the Laves phases is then . . . ABCB ABCB ABCB . . . (like the four layered hexagonal structure of SiC) and so equation (2) is valid only if the bilayer repeat is exactly four atomic planes. Since four atomic planes in this direction corresponds to approximately 5.2 Å and is comparable with the interface width, we concluded that it was not appropriate to use equation (2) but employed equation (1) and explicitly summed over every atomic plane in the superlattice.

The model adopted is then to average over each atomic plane to obtain a one dimensional model for the superlattice and to apply equation (1) to calculate the scattered intensity.

The simplest model of the interfaces between the YFe_2 and $DyFe_2$ blocks is an abrupt change in both the lattice parameters and concentration profile at the interface. This model is seldom successful, for several reasons. Firstly, there is a characteristic concentration profile across the interface, due to diffusion of the atoms at the elevated growth temperature. Secondly, the lattice mismatch between the two blocks causes a varying strain profile to exist throughout the superlattice.

To calculate the sum of equation (1) we need to know the l dependence of $f_l(\boldsymbol{Q})$ and $\boldsymbol{R}_l$. Following previous work of Jehan *et al* [6], we use tanh functions to model the concentration and strain profile of the $DyFe_2$ and YFe_2 layers as we move up through the superlattice. The concentration profile, $c_1(l)$, as a function of layer number is given by

$$c_1(l) = \frac{1}{2}\left\{1 + \sum_{S=1}^{N-2} \tanh\left[\frac{(l + 0.5 - \bar{\Lambda}S)}{\lambda_1}\right] - \sum_{S=0}^{N-1} \tanh\left[\frac{(l + 0.5 - n_1 - \bar{\Lambda}S)}{\lambda_1}\right]\right\}. \tag{4}$$

Then the form factor, $f(Q)$, is given by

$$f_l(Q) = c_1(l) f_1(Q) + [1 - c_1(l)] f_2(Q). \tag{5}$$

Similarly, the strain profile is given by

$$g_1(l) = \frac{1}{2}\left\{1 + \sum_{S=1}^{N-2} \tanh\left[\frac{l}{\lambda_2}\right] - \sum_{S=0}^{N-1} \tanh\left[\frac{(l - n_1 - \bar{\Lambda}S)}{\lambda_2}\right]\right\}, \tag{6}$$

where λ_1 determines the interface width in units of layers, λ_2 determines the strain profile also in units of layers and n_1 and n_2 are the numbers of layers of type $DyFe_2$ and YFe_2 respectively. For (1 1 0) layers in $DyFe_2$ or YFe_2 each layer is approximately 1.3 Å apart. Accordingly the lattice parameter in the growth direction, d_l, is given by

$$d_l = g_1(l) d_1 + [1 - g_1(l)] d_2, \tag{7}$$

where d_1 and d_2 are the mean lattice parameters in [1 1 0] of the $DyFe_2$ and YFe_2 blocks.

Small corrections are also made to the simulated profile by including the effects of absorption of the x-rays by the sample.

4.2. Transverse profile

The transverse scans were performed by varying the scattering vector perpendicular to the growth direction through the Bragg and superlattice reflections. This allows information about the deformation of the planes parallel to the growth direction to be extracted. Flat, undistorted planes give rise to Bragg like delta function scattering. The results of this study are more complicated because the peaks are broad in q_x and there are qualitatively two reasons for the broadening. Firstly the superlattice structure can be imperfect and this is usually described by a mosaic spread. In this case all peaks are broadened by the same angular spread.

The second cause of broadening is interfacial roughness and this gives the satellite peaks an additional width. For crystals with a small mosaic spread, the interfaces can be characterized by assuming that the interfaces display roughness, either correlated or random [18, 20]. Then providing that $q_x \ll q_z$, the intensity of the transverse scans can be written as [20]

$$I(q_x) \propto \int J_0(q_x r) \mathrm{e}^{m^2 Q_1^2 g(r)/2} r \, \mathrm{d}r, \tag{8}$$

where $J_0(x)$ is the zeroth order Bessel function, m is the order of the satellite and $Q_1 = 2\pi/\bar{\Lambda}$. The height–height correlation function, $g(r)$, of the interface is given by $g(r) = \langle (h(r) - h(0))^2 \rangle$. The functional form of $g(r)$ is often assumed to be of the form

$$g(r) = \sigma^2 (1 - \mathrm{e}^{-(r/\zeta)^\alpha}), \tag{9}$$

where ζ is the in-plane correlation length and α is the roughness parameter. This has the property that $g(r) = \sigma^2$ for large r and $g(r) = \sigma^2 (r/\zeta)^\alpha$ for small r.

The scattering from such a model has a two component lineshape, with a narrow specular component and a broader diffuse component. All of the samples in this study exhibited broad scattering with a single component because of the large mosaic spread or equivalently because the in-plane coherence length is smaller than the length for a saturation of the roughness. We therefore make a first order approximation to equation (9) and in this case one can analytically evaluate equation (8) for two specific cases, $\alpha = 1$ and 2. In the first case, the transverse lineshape is Lorentzian and the satellites broaden quadratically with increasing satellite index. This is the characteristic lineshape for a jagged local surface morphology. When $\alpha = 2$ the lineshape is Gaussian and the satellites broaden linearly with the index and the surface is smooth. In both cases the transverse profiles can be fitted under the assumption that they have a common shape. We have used a Pearson VII function that corresponds to a Lorentzian curve when the shape parameter is unity and to a effective Gaussian when the shape is large.

5. Experimental results

5.1. High resolution electron microscopy measurements

The HREM measurements were performed using a JEOL 4000EX operating at 400 keV, with a point resolution of 0.16 nm. Figure 5 shows a typical image through several bilayers of a $DyFe_2$–YFe_2 superlattice. This image confirms that the superlattices show a high degree of modulation and it also shows that the interface width is consistent with the interface widths deduced from the x-ray diffraction analysis. More detailed analysis was not pursued because of the possibility that defects (including structural damage and H incorporation) could be introduced during HREM sample preparation of these reactive materials.

5.2. X-ray scattering—structural properties

5.2.1. Longitudinal profile. Initially for sample SL932, two sets of measurements were made of the scattered intensity observed when the wavevector transfer was varied longitudinally through the 2 2 0 Bragg reflection. One set used a three crystal configuration and the other used a two crystal configuration, with a secondary slit size of 0.3 mm. The results of these measurements are shown in figure 6.

As expected, the agreement between the two sets of measurements is very good. However, the scattered intensity observed using a three crystal configuration was considerably weaker than when using the two crystal configuration. For this reason, all of the subsequent measurements were made using the latter configuration. However, figure 6 shows that the

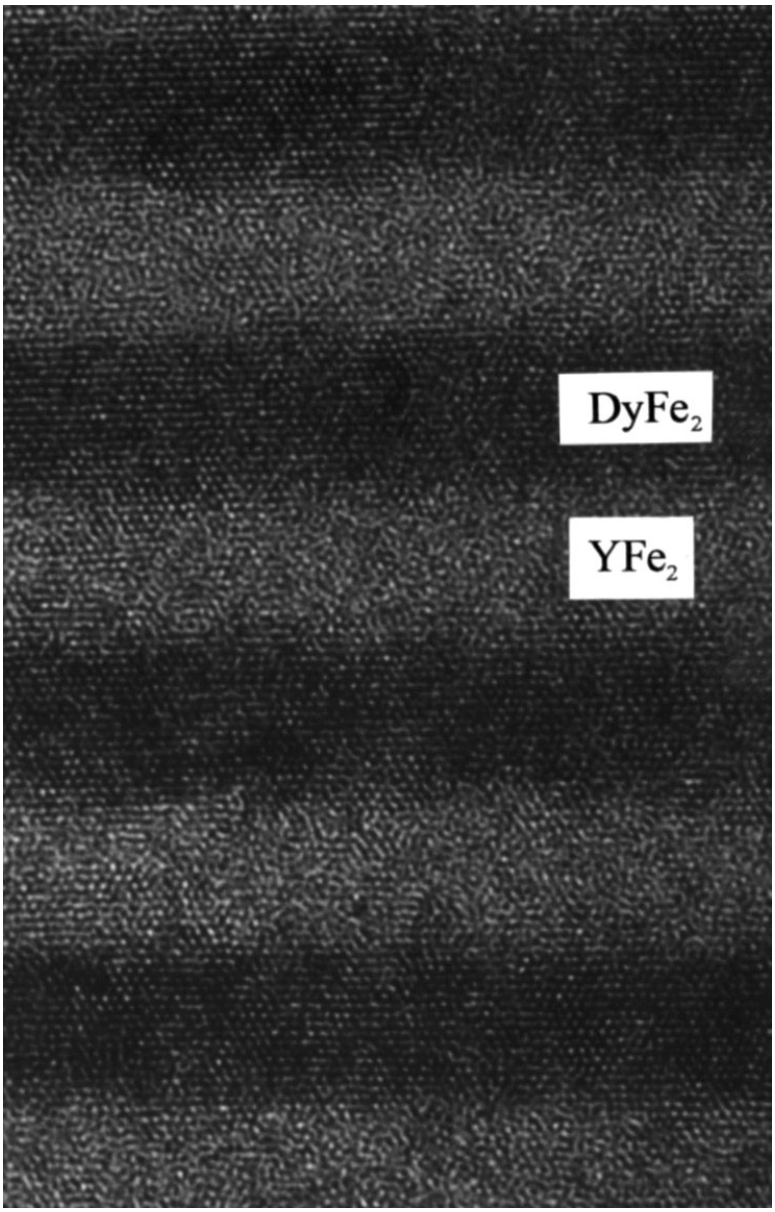

Figure 5. A HREM image of a section through a Laves phase superlattice of $DyFe_2/YFe_2$. The nominal bilayer repeat distance is 100 Å in the [1 1 0] growth direction and the zone axis is [1 $\bar{1}$ 1], perpendicular to the growth direction. The image is taken along an in-plane ⟨1 1 1⟩ direction.

width of the main Bragg reflection is considerably narrower for the three crystal configuration than when using the two crystal configuration. This is because the resolution function in the q_z direction is larger for the two crystal configuration. Therefore to accurately measure the coherence length, ξ, the observed peak width, Δq_z, needs to be corrected using

$$\Delta q_z^2 = (\Delta q_z^{\mathrm{corr}})^2 + \Delta_{\mathrm{IR}}^2, \tag{10}$$

where Δ_{IR} is the broadening due to the instrumental resolution function and $\Delta q_z^{\mathrm{corr}}$ is the

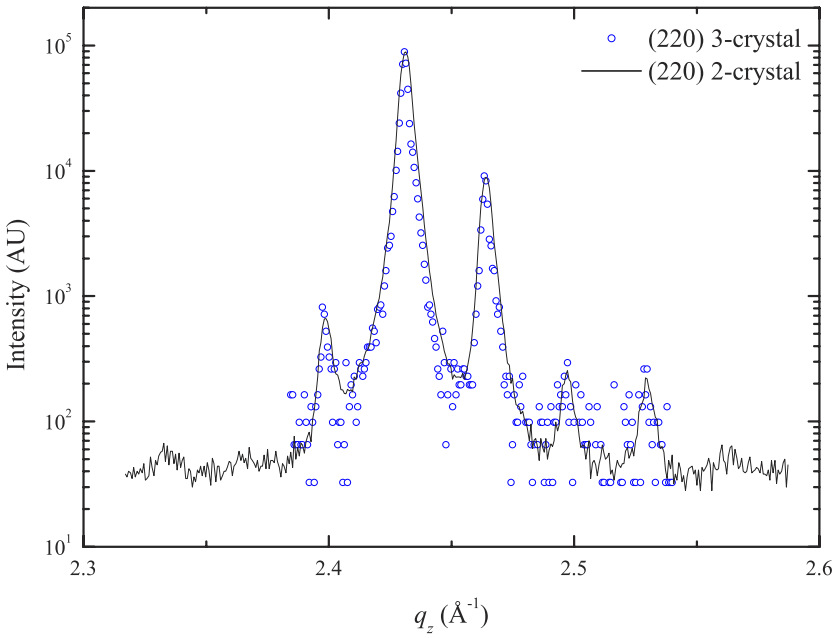

Figure 6. A comparison of the scattered intensity observed when the wavevector transfer was varied longitudinally through the 2 2 0 reflection for two different x-ray configurations. The data collected using the three crystal configuration has been rescaled to the data from the two crystal measurements.

resolution corrected width. The coherence length is then calculated using

$$\xi = \frac{2\pi}{\Delta q_z^{\mathrm{corr}}}. \tag{11}$$

For this analysis to be valid, the corrected longitudinal FWHM of the main Bragg peak must be independent of the order of reflection measured. Most studies usually just measure one reflection and its associated satellites, so this criterion cannot be verified. In this study we have measured three reflections; the scattered intensity observed when the wavevector transfer was scanned through the Bragg reflections longitudinally by varying the q_z component of the scattering vector for selected samples is shown in figure 7. Analysis of these results shows that the width of main Bragg peak *is* dependent on the order of reflection and so strictly speaking a unique value for the coherence length cannot be found using equation (11). Typical values for the resolution corrected FWHM of the main Bragg peak for these reflections for sample 932 are $\Delta q_z(2\,2\,0) = 0.002\,68(0.000\,04)$ Å^{-1}, $\Delta q_z(4\,4\,0) = 0.004\,91(0.000\,06)$ Å^{-1} and $\Delta q_z(2\,6\,\bar{2}) = 0.011\,86(0.000\,02)$ Å^{-1}. However, for comparison with other studies, we have included the results of calculating the coherence length from the 2 2 0 reflection, table 1, along with the rocking curve FWHM. The reasons for the dependence of the longitudinal width as a function of q_z are discussed in the following sections.

Before any detailed analysis of the lineshape shown in figure 7 is made, a few general conclusions can be drawn from the observed profile. Firstly, these profiles display a main Bragg peak that is highest in intensity. This peak arises due to the scattering from planes that have an average spacing $\bar{d}$. Secondly, all of the samples examined showed a large number of subsidiary peaks or superlattice peaks. The presence of these peaks gives a qualitative indication that these samples exhibit a high degree of modulation. The superlattice peaks are

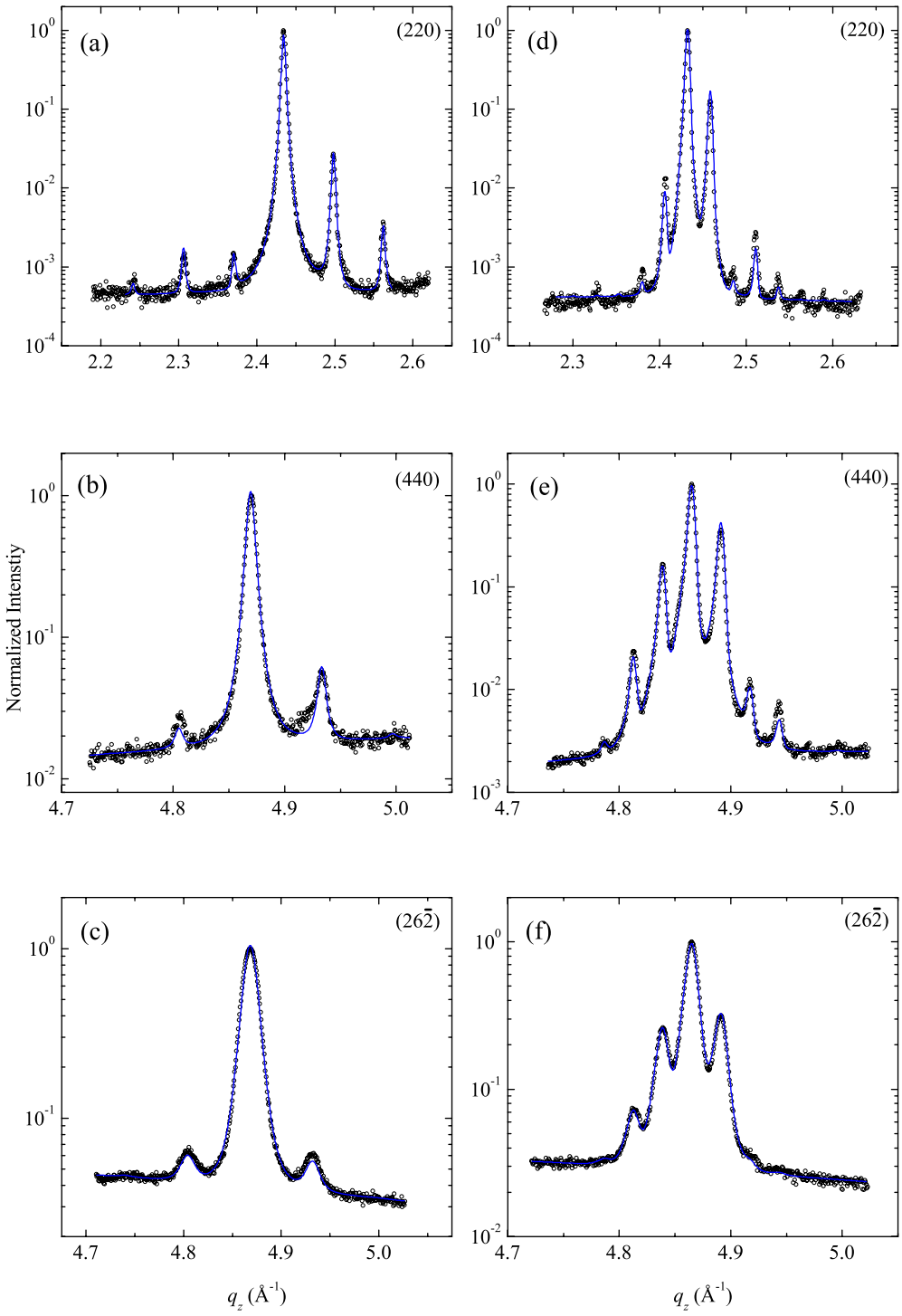

Figure 7. The observed scattered intensity as the wavevector transfer was varied longitudinally for various reflections. The superlattice samples are of structure $[t_1$ Å $DyFe_2/t_2$ Å $YFe_2]_N$. Sample SL989 $[70/30]_{60}$ is shown in (a)–(c) and SL1003 $[150/100]_{50}$ in (d)–(f). The solid curve is a fit to the data based on the models described in the text.

Table 2. The resolution corrected FWHM of the 2 2 0 Bragg reflection and associated satellites of the longitudinal scans for sample SL932 $[100/100]_{40}$.

Satellite index, m	-1	0	1	2	3
FWHM (Å^{-1})	0.0029	0.002 68	0.0025	0.0025	0.0032
Error (Å^{-1})	0.0015	0.000 04	0.0002	0.0037	0.0049

asymmetrical about the main Bragg peak, which is evidence for a varying concentration *and* strain profile in the superlattice. Also the width of the main Bragg peak and superlattice peaks remains largely constant, table 2, which shows that the deviations from the average bilayer repeat distance, $\bar{\Lambda}$, are small. The mean bilayer repeat distance, $\bar{\Lambda}$, can be obtained from the spacing of the satellite peaks.

Superlattice satellites were also observed around the $1\,7\,\bar{3}$ and $2\,6\,\bar{2}$ reflections. The results for the $2\,6\,\bar{2}$ reflection are shown in figures 7(c) and (f) and this reflection has an in-plane component, q_x, to the wavevector transfer. The presence of satellites around this reflection shows that the superlattices exhibit a high degree of in-plane coherence and that the regular stacking sequence of the planes is preserved.

5.2.2. Fitting x-ray scattering data from superlattices. The cubic Laves phases grow in an FCC lattice, with a six atom rare earth–transition metal basis. A calculation of the structure factor reveals that some reflections are more sensitive to the rare earth atoms, while others are more sensitive to the transition metal atoms. In particular, for a pure film of $DyFe_2$ the 2 2 0 reflection depends only on the scattering from the dysprosium atoms, while the 4 4 0 reflection is sensitive to a mixture of the scattering from the dysprosium and iron atoms, while the $2\,6\,\bar{2}$ reflection depends only on the scattering from the iron atoms. This means that these experimental lineshapes contain different information and so therefore all these peaks should be simultaneously fitted to a common model.

Non-linear fitting of superlattice data with a conventional Levenberg–Marquardt fitting routine can often result in difficulty. The results can depend upon the initial values of the parameter vector, $\boldsymbol{p}$, because this algorithm is guided by the form of the error function in the parameter space and has a tendency to become trapped in local minima. This can often result in numerous abortive fitting attempts. This is usually not a problem when the parameter space is relatively small and when the fitting function can be quickly evaluated. The model described here is relatively slow to evaluate since it performs a sum over numerous bilayer repeats and performs the calculation simultaneously for several Bragg reflections. In addition the number of parameters, m, required for this model was typically 115, of which about 30 were variable. The complexity of the model means that the m dimensional error function space that had to be searched was very large. Finally, the complication of simultaneously fitting several reflections means that a conventional Levenberg–Marquardt algorithm would not be an effective way of finding the global minimum of the error function. Hence we used an alternative fitting routine, a DEA, and found that it was more reliable in locating a global minimum.

The DEA has the advantage that convergence to a global minimum of the error function is virtually guaranteed, provided that a suitable error function for the data is selected. The error function that we used was of the form

$$E = \sum_{j=1}^{n} [\log I_{\text{mod}_j} - \log I_{\text{expt}_j}]^2, \tag{12}$$

because it was found to cope well with the lineshapes that spanned several orders of magnitude. The DEA algorithm is described in detail by Wormington *et al* [21] and is outlined below.

Firstly, an initial guess is made for a parameter vector $\boldsymbol{p}_0 = [p_1, p_2, \ldots, p_n]$ that contains the n fitting variables. Then a set of parameter vectors $\boldsymbol{P} = [\boldsymbol{p}_0, \boldsymbol{p}_1, \ldots, \boldsymbol{p}_{m-1}]$ is created. This has a population m and the vectors $\boldsymbol{p}_1, \ldots, \boldsymbol{p}_{m-1}$ are created by randomly selecting the value of each parameter $p_1, \ldots, p_n$ that make up $\boldsymbol{p}_1$ etc from within upper and lower limits. The intensity, $I(q_z; \boldsymbol{p})$, is then calculated for each population member and the error function calculated by comparing the model to the data using equation (12). The best fit member of the population is assigned to $\boldsymbol{b}$. A better solution is obtained by selecting two random members of the population $\boldsymbol{P}$, $\boldsymbol{p}_\mathrm{a}$ and $\boldsymbol{p}_\mathrm{b}$. Then their difference is computed and the best vector $\boldsymbol{b}$ is mutated according to

$$\boldsymbol{b}' = \boldsymbol{b} + k_\mathrm{m}(\boldsymbol{p}_\mathrm{a} - \boldsymbol{p}_\mathrm{b}), \tag{13}$$

where k_m is a mutation constant, that was set to 0.7 in our calculations. Finally a new trial vector $\boldsymbol{t}$ is created by starting with the randomly chosen jth parameter and either choosing it from the $\boldsymbol{b}'$ vectors or as $\boldsymbol{p}_0$. This is decided by taking a random number from a uniform (0, 1) distribution. If the random number is less than k_r, then the jth parameter is chosen from the $\boldsymbol{b}'$ vectors, whereas if it is greater than k_r, then the parameter is chosen as $\boldsymbol{p}_0$. k_r was set to 0.5. The error function is then computed and this trial vector is compared to a randomly chosen member of the population. If the fit is better, then this member is replaced by the trial vector and the whole process is repeated. All of the calculations and fitting routine were performed using a FORTRAN code and this method provided a fast way of computing the large sums required to calculate the simulated profile.

The fitting procedure was terminated when there was convergence of all the population members, with the result that the trial vector $\boldsymbol{t}$ produced a lineshape that was indistinguishable from the best fit vector. The errors were estimated by performing a grid search around the minimum found by the DEA. The errors in each parameter were then estimated at a 5% level of the error function.

The parameters allowed to vary during the fitting procedure were the mean lattice parameters of the $DyFe_2$ and YFe_2 blocks, d_1 and d_2, the corresponding numbers of layers of these blocks, n_1 and n_2, and the concentration (λ_1) and strain (λ_2) profiles of the superlattice. The other variable parameters were the gradient and intercepts of the background at each reflection and also the four parameters required to define the Pearson VII functions that were convolved with the raw simulations. This function was required to take account of the instrumental resolution and any imperfections of the superlattice not included in the model that give rise to broadenings of the reflections.

5.2.3. Fitting results. There is excellent agreement between the results of the fitting and experimental results as shown for samples SL989 and SL1003 in figure 7. The results of fitting the longitudinal scans to the model described in section 4.1 are presented in table 3 and these give good agreement with the nominal thicknesses. The measured structure has been deduced from the number of layers and average spacing of the $DyFe_2$ and YFe_2 blocks.

Table 3 also shows the fitted values of the concentration profile, λ_1, and strain profile, λ_2. The interface widths deduced from the fitting are relatively large. In order to clearly demonstrate the form of this profile, the strain profile for sample SL989 is shown in figure 8. For this particular sample, the fitted value of the strain profile was $\lambda_2 = 10$ layers. This shows that the interfaces have a width of the order of 13 Å. The concentration profile is slightly sharper for this sample, of the order of 9 Å. The HREM image presented in figure 5 shows that, over a particular $\sim(300 \times 300)$ Å area of sample, the interface width is consistent with that deduced from the x-ray diffraction.

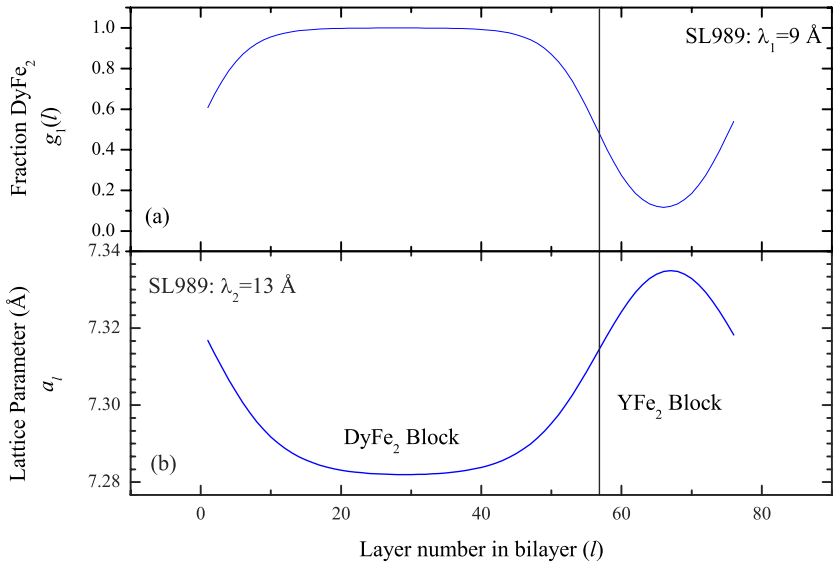

Figure 8. (a) The concentration profile, and (b) strain profile deduced from the fitted data for sample SL989 $[70/30]_{60}$. The vertical line marks the position of an abrupt interface for a sample with $\lambda = 0$.

Table 3. The structural parameters of the $DyFe_2/YFe_2$ superlattices as determined by x-ray diffraction at room temperature. The parameters given in the table were obtained from simultaneous fits of the three measured diffraction profiles by the scattering model described in section 4.1. The errors are estimated piecewise at a 5% level of the error function.

	Structure		λ_1	λ_2
Sample	Nominal	Measured	(Å)	(Å)
932	$[100/100]_{40}$	$[95.26/97.32]_{40}$	31(1)	2(5)
933[a]	$[150/150]_{40}$	$[145.25/137.40]_{40}$	20(6)	21(3)
955[a]	$[250/150]_{30}$	$[265.04/153.05]_{30}$	39(10)	18(10)
989	$[70/30]_{60}$	$[73.37/24.41]_{60}$	9(1)	13(2)
990	$[50/70]_{60}$	$[55.26/67.39]_{60}$	14(2)	12(2)
1003	$[150/100]_{50}$	$[151.86/88.35]_{50}$	19(6)	19(2)

[a] Determined from 2 2 0 and 4 4 0 reflections only.

5.2.4. Strain analysis. The positions of the measured reflections permitted the in-plane and out-of-plane lattice constants to be measured. The [1 1 0]–[1 $\bar{1}$ 1] scattering plane, which contains a high density of suitably inclined reflections, was used to determine the in-plane lattice constant along [1 $\bar{1}$ 1]. In order to check for in-plane anisotropy, for sample SL1003 a measurement of the 5 5 $\bar{3}$ reflection enabled the a_{001} lattice parameter to be determined. Table 4 lists the lattice parameters measured both out-of-plane (for each superlattice component and the average) and in-plane. These values should be compared with the bulk parameters equal to 7.325 Å for $DyFe_2$ and 7.363 Å for YFe_2. A single value found in each case for the in-plane parameter means that the $DyFe_2$ and YFe_2 component layers are strained to be pseudomorphic. However, a large tensile strain has been imposed on the whole superlattice stack. These results are consistent with previous reports of strains in epitaxial RFe_2 single films and bilayers [22–24]. The dominant tensile strain is introduced during cooling of the

Table 4. The average lattice parameters for the $DyFe_2$ blocks (a_1) and YFe_2 blocks (a_2) deduced from the simultaneous fits of three Bragg reflections to the model described in the text. $\bar{d}$ is the weighted average lattice parameter defined as $\bar{a} = \sqrt{2}(n_1 d_1 + n_2 d_2)/(n_1 + n_2)$. Sample 1002 is a 10 000 Å layer of $DyFe_2$.

Sample	a_1 (Å)	a_2 (Å)	$\bar{a}$ (Å)	$a_{1\bar{1}1}$ (Å)	a_{001} (Å)
932	7.282(0.001)	7.340(0.001)	7.311(0.001)	7.389(0.001)	—
933	7.271(0.002)	7.340(0.002)	7.305(0.002)	—	—
955	7.278(0.001)	7.337(0.001)	7.300(0.001)	—	—
989	7.281(0.002)	7.356(0.005)	7.300(0.005)	7.392(0.001)	—
990	7.270(0.001)	7.332(0.001)	7.305(0.001)	7.394(0.001)	—
1003	7.280(0.001)	7.349(0.001)	7.305(0.001)	7.394(0.001)	7.388(0.001)
1002	—	—	7.310(0.001)	7.355(0.001)	7.376(0.001)

Table 5. Thermal expansion coefficients of sapphire [25].

Compound	Axis	T_0	A (10^{-6} K^{-1})	B (10^{-9} K^{-1})
Al_2O_3	c	273	6.582	4.995
Al_2O_3	a	273	5.425	5.534

sample from the growth temperature to ambient and is a result of substrate clamping by the sapphire, which has a thermal expansion coefficient considerably lower than that of RFe_2. Our results on superlattice sample 1003 differ from those of Mougin *et al* [22] in that the strain is not exactly isotropic in the plane. In fact, in-plane anisotropy would be expected with the substrate-clamping model because sapphire has $R\bar{3}c$ symmetry and is therefore not isotropic within the (1 1 0) plane. The thermal expansion coefficients, α, of Al_2O_3 parallel and perpendicular to the c-axis differ by some 10%, as shown in table 5 and are calculated using $\alpha = A + B(T - T_0)$. This difference has been ignored in previous models [22]. In order to investigate the question of anisotropic strain using a simpler RFe_2 structure and to compare directly with previous studies, the lattice constants of a single layer of $DyFe_2$ of 10 000 Å thickness were measured, sample 1002 (table 4). The anisotropy in this sample is found to be much more significant and is of different sign to the small anisotropy measured in SL1003. In fact the sign of the anisotropy measured in the single $DyFe_2$ film is consistent with the proposed model of lattice clamping by the anisotropic sapphire substrate (see table 5), although the magnitude of the measured anisotropy is larger than would be predicted if the $DyFe_2$ was assumed to be relaxed at the growth temperature. The origin of the small anisotropy of opposite sign in the superlattice sample, SL1003, is not clear. Quantitative analysis of these systems is made more difficult by the scarcity of data on thermal expansion coefficients of RFe_2 compounds. Values of 12×10^{-6} K^{-1} (300 K) and 16×10^{-6} K^{-1} (820 K) are quoted by previous authors [22, 24] as general values for RFe_2 compounds, but it is likely that these values will depend on the rare earth element and there could also be magnetoelastic effects and possible anisotropy in some of the RFe_2 compounds.

5.2.5. Transverse profile. Typical scans when the wavevector transfer was varied perpendicular to the sample surface by varying the q_x component are shown in figure 9.

The presence of a single component lineshape in these scans shows that there is a common in-plane lattice parameter for both the YFe_2 and $DyFe_2$ blocks. This result is to be expected since the mismatch of bulk $DyFe_2$ relative to YFe_2 is given by $\Delta a/a = -0.516\%$ [26], so the critical thickness for the introduction of dislocations to relax the strain is expected to be larger

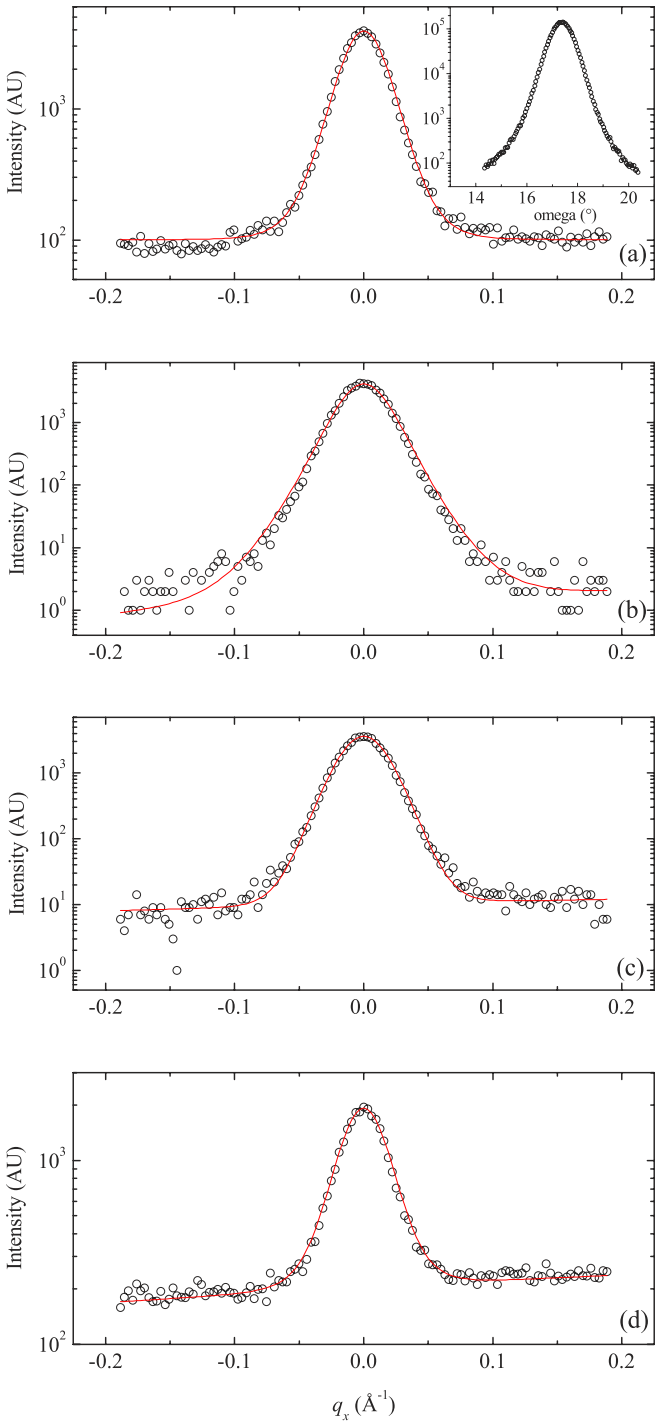

Figure 9. The scattered intensity observed when the wavevector transfer was varied transversely through the main peak and superlattice peaks for the 2 2 0 reflection for sample SL1003 $[150/100]_{50}$. (a) Satellite −1 and (inset) a rocking curve for the 2 2 0 reflection, (b) the main Bragg peak, (c) satellite +1, (d) satellite +3.

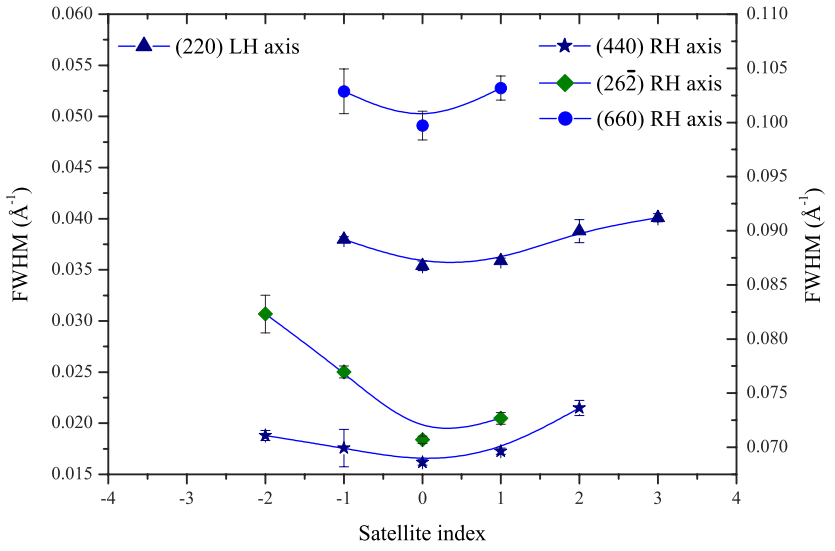

Figure 10. Results of fitting the transverse scans to a common shape for sample SL1003 $[150/100]_{50}$.

than the layer thickness of the sample. Much higher strains are needed before relaxation of each block takes place, as has been shown to occur in holmium–scandium superlattices [27], where the in-plane mismatch $\Delta a/a = -7.51\%$, which results in partial relaxation of the strain between the layers.

These scans and other similar scans for the 4 4 0 and 2 6 $\bar{2}$ reflections were simultaneously fitted to a single Pearson VII function with a linear background. This was achieved using the DEA described in section 5.2.2. All of the scans were fitted with a common shape since the shape of the peak is characteristic of the $DyFe_2$–YFe_2 interface and the mosaic spread. The common peak shape determined from the fit for this sample was 3.3. The widths were then determined as a function of satellite index and the results are shown in figure 10. They show that the width of the peaks is dominated by the mosaic width that varies linearly as a function of q_z. This suggests that there is a high density of dislocations in the superlattice giving rise to domains with different tilts. A secondary effect is the increase of the widths with the satellite index. It has been shown that the contribution of the interface roughness to the widths of the first and subsequent satellites of a superlattice with interfacial roughness is given by $\Gamma_n/\Gamma_1 = n^{2/\alpha}$ [20] where n is the satellite index, Γ is the width of the scan and α is the roughness exponent. Therefore our results suggest that there is some correlated roughness present at the interfaces of these Laves phase superlattices. A similar analysis of the transverse scans of the other superlattice samples was also performed and these results were qualitatively similar to those discussed previously, showing that the roughness was common to all the superlattice samples in this study.

5.2.6. Area plots. The scattering around the 2 2 0 reflection was measured for sample SL1003 in order to investigate further the interfacial structure of the sample. These results are displayed in figure 11. The intensity has been plotted on a log scale. This shows a main Bragg peak that is highest in intensity and a number of subsidiary peaks either side of the main peak. This area plot shows that the peaks are rather streak like in the in-plane direction. The streaks show that there is some correlated roughness present in these superlattice samples.

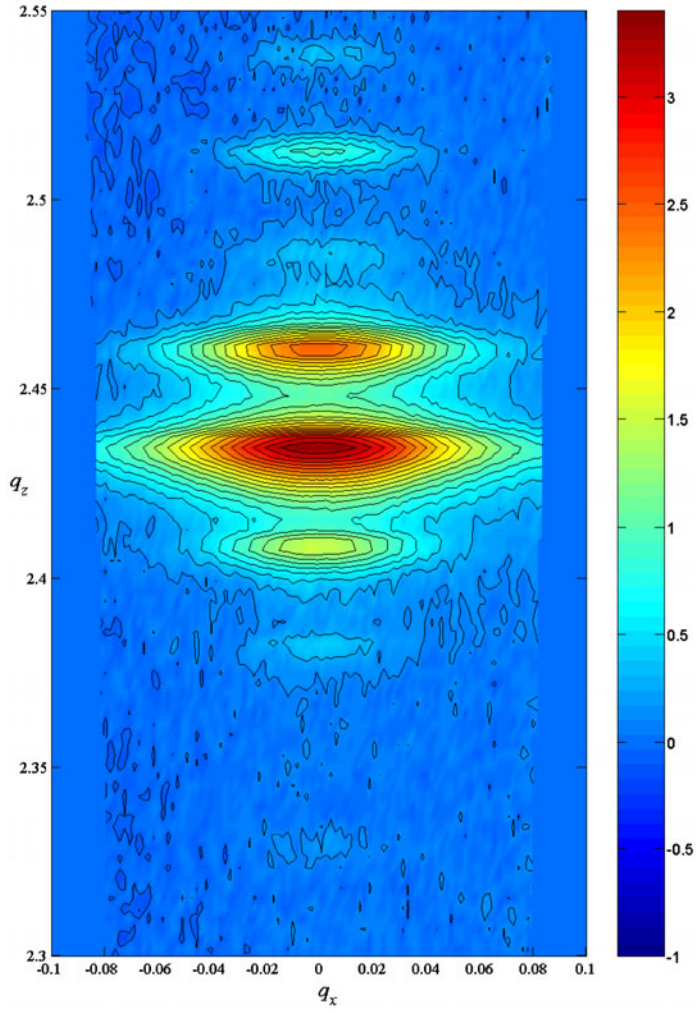

Figure 11. A detailed contour plot around the 2 2 0 reflection for superlattice sample SL1003 $[150/100]_{50}$. The contours are on a logarithmic scale and the units of q_x and q_z are Å^{-1}.

6. Conclusions and discussion

We have presented the results of a study on the structural properties of a series of high quality Laves phase superlattice samples grown by MBE. We have used a DEA algorithm to simultaneously fit three longitudinal scattering profiles for each sample to a common model and to show that the agreement between the model and experiment is excellent, over three orders of magnitude and for all the reflections. The superlattice satellites have a longitudinal width that remains largely constant for the main peak and superlattice peaks, which shows that the fluctuations around the mean bilayer length $\bar{\Lambda}$ are small [18]. This allows us to extract an estimate for the interface width for these superlattices. Typically this is of the order of 10 Å. The value deduced for the interface width in this way is consistent with an estimate of the interface width made from HREM measurements.

The longitudinal profile showed a dependence of the FWHM of the main Bragg peak as a function of q_z. This result shows that there is a non-uniform strain profile throughout

the whole superlattice structure. The models presented encompassed this by convolving the simulated lineshape with a Pearson VII function, the width and shape being determined from the experimental data. Future models should be able to take this effect into account by including a varying strain profile throughout the superlattice in addition to the bilayer concentration and strain profiles. This effect of the strain profile varying throughout the whole superlattice is probably a consequence of the dislocations introduced in the initial stages of the growth of the samples and also because the first few bilayer repeats were grown at 600 °C and the temperature reduced gradually to 450 °C over the course of the next few bilayer repeats. This may give rise to a varying strain profile throughout the superlattice. The width of the $2\,6\,\bar{2}$ reflection was found to be considerably larger in the longitudinal direction than that of the 4 4 0 reflection. These reflections both have the same q_z component to the wavevector transfer, so a varying strain profile throughout the whole superlattice cannot explain this. Measurements of the resolution function show that this effect cannot be explained as because of a rotation of the resolution ellipsoid. Therefore it is more likely that these samples exhibit some disorder in the stacking sequence of the planes in the [1 1 0] direction.

We have also measured the in-plane lattice parameters and shown that the strains are almost uniform in the epitaxial plane. The lattice parameter in the growth direction is about 7.30 Å which is considerably smaller that the bulk values for $DyFe_2$ and YFe_2. This is a direct result of the epitaxial strains expanding the in-plane lattice constants relative to the bulk compounds.

Comparison of the lattice constants of a 10 000 Å thick layer of $DyFe_2$ grown in a similar manner to the Laves phase superlattices shows that this sample exhibits a non-uniform in-plane strain. This result can be qualitatively explained by the different thermal expansion coefficients of sapphire and $DyFe_2$ and the anisotropy of sapphire in $(1\,1\,\bar{2}\,0)$.

For the superlattices, transverse scans performed through the main peak and subsidiary satellite peaks shows that the peak width is dominated by a mosaic crystal effect that arises due to the high density of dislocations that partially relax the strain in the superlattice. The mosaic spreads are typically 0.9°, while the superlattice coherence length, ξ, is typically 2000 Å.

These results show that, despite the complex growth process, these Laves phase superlattices are of high quality. This study also demonstrates that for complex superlattice structures, several Bragg reflections should be measured and simultaneously fitted to a model if an accurate description of the structure is required. The large parameter space being searched shows the need for a fitting routine that is capable of avoiding being trapped in local minima and the DEA algorithm is shown to be an extremely effective way of performing a non-linear least squares fit using a Rietveld refinement.

Acknowledgments

This work was funded by the UK Engineering and Physical Sciences Research Council (EPSRC). We would also like to thank R A Cowley and A Yu Babkevich for useful discussions and for comments on this manuscript.

References

[1] Coey J M D and Skomski R 1993 New magnets from interstitial intermetallics *Phys. Scr.* T **49** 315–21
[2] Buschow K H J 1977 Intermetallic compounds of rare-earth and 3d transition metals *Rep. Prog. Phys.* **40** 1179–256
[3] Swaddling P P, Cowley R A, Ward R C C and Wells M R 1996 Magnetic structures of holmium–lutetium alloys and superlattices *Phys. Rev.* B **53** 6488–98

[4] Majkrzak C F, Kwo J, Hong M, Yafet Y, Gibbs D, Chen C L and Bohr J 1991 Magnetic rare-earth superlattices *Adv. Phys.* **40** 99–189
[5] Ward R C C, Wells M R, Bryn-Jacobsen C, Cowley R A, Goff J P and McMorrow D F 1996 MBE growth and characterisation of light rare-earth superlattices *Thin Solid Films* **275** 137–9
[6] Jehan D A, McMorrow D F, Cowley R A, Ward R C C, Wells M R and Hagmann N 1993 Magnetic structure of holmium–yttrium superlattices *Phys. Rev.* B **48** 5594–606
[7] Ritter C 1989 Polarised neutron study of the magnetic ordering in the simple alloy YFe_2 *J. Phys.: Condens. Matter* **1** 2765–9
[8] Dumesnil K, Dutheil M, Dufour C and Mangin Ph 2000 Spring magnet behaviour in $DyFe_2$–YFe_2 Laves phase superlattices *Phys. Rev.* B **62** 1136–40
[9] Sawicki M, Bowden G J, de Groot P A J, Rainford B D, Beaujour J M L, Ward R C C and Wells M R 2000 Exchange springs in antiferromagnetically coupled $DyFe_2$–YFe_2 superlattices *Phys. Rev.* B **62** 5817–20
[10] Sawicki M, Bowden G J, de Groot P A J, Rainford B D, Beaujour J M L, Ward R C C and Wells M R 2000 Engineering coercivity in epitaxially grown (110) films of $DyFe_2$–YFe_2 superlattices *Appl. Phys. Lett.* **77** 573–5
[11] Beaujour J M L, Gordeev S N, Bowden G J, de Groot P A J, Rainford B D, Ward R C C and Wells M R 2001 Negative coercivity in epitaxial grown (110) $DyFe_2$–YFe_2 superlattices *Appl. Phys. Lett.* **78** 964–6
[12] Beaujour J M L, Bowden G J, Gordeev S, de Groot P A J, Rainford B D, Ward R C C and Wells M R 2001 Exchange springs in YFe_2 dominated $DyFe_2$–YFe_2 superlattices *J. Magn. Magn. Mater.* **226–230** 1870–2
[13] Gordeev S N, Beaujour J M L, Bowden G J, de Groot P A J, Rainford B D, Ward R C C and Wells M R 2001 Spin configurations and negative coercivity in epitaxially grown $DyFe_2$–YFe_2 superlattices *J. Appl. Phys.* **89** 6828–30
[14] Beaujour J M L, Bowden G J, Gordeev S, de Groot P A J, Rainford B D, Sawicki M, Ward R C C and Wells M R 2001 Effect of exchange springs on the coercivity of $DyFe_2$–YFe_2 superlattices *J. Magn. Magn. Mater.* **226–230** 1714–6
[15] Gordeev S N, Beaujour J M L, Bowden G J, Rainford B D, de Groot P A J, Ward R C C, Wells M R and Jansen A G M 2001 Giant magnetoresistance by exchange springs in $DyFe_2$–YFe_2 superlattices *Phys. Rev. Lett.* **87** 1–4
[16] Oderno V, Dufour C, Dumesnil K, Mangin Ph and Marchal G 1996 Epitaxial growth of (110) $DyFe_2$, $TbFe_2$ thin films by molecular beam epitaxy *J. Cryst. Growth* **165** 175–8
[17] McMorrow D F, Swaddling P P, Cowley R A, Ward R C C and Wells M R 1993 The chemical structure of rare earth superlattices: a high-resolution x-ray scattering study *J. Phys.: Condens. Matter* **5** 6553–67
[18] Fullerton E E, Pearson J, Sowers C H, Bader S D, Wu X Z and Sinha S K 1993 Interfacial roughness of sputtered multilayers: Nb/Si *Phys. Rev.* B **48** 17432–44
[19] Ibers J A and Hamilton W C (ed) 1974 *The International Tables for Crystallography* vol 4 (Birmingham: Kynoch)
[20] Yan X and Egami T 1993 Interfacial structure of Co/Pt multilayers *Phys. Rev.* B **47** 2362–7
[21] Wormington M, Panaccione C, Jatney K M and Bowen D K 1999 Characterization of structures from x-ray scattering data using genetic algorithms *Phil. Trans. R. Soc.* A **357** 2827–48
[22] Mougin A, Dufour C, Dumesnil K, Maloufi N and Mangin Ph 1999 Strain in single-crystal RFe_2 thin films *Phys. Rev.* B **59** 5950–9
[23] Huth M and Flynn C P G 1998 Effects of heteroepitaxial strain on Laves phases $TbFe_2$ and $DyFe_2$ *J. Appl. Phys.* **83** 7261–3
[24] Wang C T, Clemens B M and White R L 1996 Effects of substrate on the magnetic properties of epitaxial $TbFe_2$ films *IEEE Trans. Magn.* **32** 4752–4
[25] Krishnan R S, Srinivasan R and Devanarayanan S 1979 *Thermal Expansion of Crystals* (*International Series in the Science of the Solid State* vol 12) 1st edn (Oxford: Pergamon)
[26] Wyckoff R W G 1965 *Crystal Structures* (New York: Interscience)
[27] Bryn-Jacobsen C, Cowley R A, McMorrow D F, Goff J P, Ward R C C and Wells M R 1997 Structural and magnetic properties of holmium–scandium alloys and superlattices *Phys. Rev.* B **55** 317–29